Hexagonal Arrays of Cylindrical Nickel Micro-structures for Improved Oxygen Evolution Reaction

Michael T.Y. Paul[1], Brenden B. Yee[1], David R. Bruce[2], Byron D. Gates[1]*

1) Department of Chemistry, Simon Fraser University, 8888 University Drive, Burnaby, B.C. V5A 1S6, Canada

2) ZincNyx Energy Solutions, 8765 Ash St #1, Vancouver, B.C. V6P 6T3, Canada

ABSTRACT: Fuel cell systems are of interest for a wide range of applications, in part for their utility in power generation from non-fossil fuel sources. However, the generation of these alternative fuels, through electrochemical means, is a relatively inefficient process due to gas passivation of the electrode surfaces. Uniform micro-structured nickel surfaces were prepared by photolithographic techniques as a systematic approach to correlate surface morphologies to their performance in the electrochemically driven oxygen evolution reaction (OER) in alkaline media. Hexagonal arrays of micro-structured Ni cylinders were prepared with features of proportional dimensions to the oxygen bubbles generated during the OER process. Recessed and pillared features were investigated relative to planar Ni electrodes for their influence on OER performance and, potentially, bubble release. The arrays of cylindrical recesses were found to exhibit an enhanced OER efficiency relative to planar nickel electrodes. These micro-structured electrodes had twice the current density of the planar electrodes at an overpotential of 100 mV. The results of these studies have important implications to guide the preparation of more efficient fuel generation by water electrolysis and related processes.

1. Introduction

In this study, arrays of cylindrical Ni micro-structures were prepared on top of planar Ni electrodes to seek a structure property correlation for guiding the preparation of electrode designs that improve the efficiencies of electrolysis systems. In an effort to reduce our dependence on fossil fuels and our carbon emissions, the use of alternative methods for energy generation that are cleaner and more easily renewed, such as through capturing solar energy and harnessing wind energy, have become increasingly prominent in recent years.[1-7] However, due to the intermittent nature of these alternative energy sources, a reliable method is required for saving excess power for storage or transportation.[4,8] Potential solutions to our storage needs include fuel cells and batteries, such as lead acid, nickel metal-hydride, and lithium ion batteries.[4,5,8-10] Fuel cells that utilize gaseous fuels, such as hydrogen, have been demonstrated to be a cost effective power source.[9-11] This type of fuel cell also has the advantage of decoupling their power generation (i.e. fuel consumption) and fuel generation systems, so the systems can be effectively charged while simultaneously generating power.[12] Stored hydrogen fuel, for example, can be transported to different locations for use in proton exchange membrane fuel cells (PEMFCs).[13-14] However, it remains a challenge to expand fuel storage capacity, as well as to provide safe long-term storage of hydrogen.[4,8-12] Due to such limitations, the use of PEMFCs have been predominantly focused on mobile systems with a reduced capacity (e.g., forklifts, cars, and buses) relative to the capacity required to buffer the differences between the cycles of power generation from alternative means and the continuous demands of the grid.[4,8-9] Other types of fuel cells, such as the zinc-air fuel cell (ZAFC), are being developed as alternative stationary power needs. The ZAFC utilizes metallic zinc pellets as the fuel source. One advantage of this system is that its capacity can be easily expanded by increasing the size of its fuel reservoir and the zinc fuel can be stored as an aqueous suspension of particulate metal solids for relatively safe use in residential or industrial applications.[15-17]

A common limitation to all power conversion processes are the inefficiencies in these processes. In fuel cells, these limitations reside, in part, in the processes required to generate the fuel. Inefficiencies in fuel generation are related to the build-up of gases as they are formed at the electrode surfaces. Water electrolysis generates hydrogen and oxygen at the cathode and anode, respectively, which can be used as fuels in PEMFCs.[4,6,8-9] The ZAFCs utilize electrochemical methods to produce the required fuel of particulate zinc[15-17], and simultaneously the oxygen evolution reaction (OER) generates oxygen gas at the anode.[16-17] The inefficiency of these electrochemical fuel production processes can be observed with a drastic increase in resistance of these systems as gas bubbles are formed at the electrode surfaces.[18-20] The formation of persistent bubbles on the electrode surfaces can impede ionic transport and block the catalytic active sites.[18-20] Catalyst materials and electrodes with larger surface areas can increase OER activity, but are more susceptible to significant increases in resistance as relatively large amounts oxygen are generated

at these electrodes.[21-23] The efficiency of these electrochemical processes may be improved by enhancing the removal of bubbles from the surfaces of these electrodes. Improving the efficiency of fuel generation is valuable for both water electrolysis and rechargeable metal-air systems that depend on anodic OER processes. Further optimization to the design of the interface between the electrode and the electrolyte to promote release of gas bubbles could improve the overall efficiency of these fuel cell systems.

Electrode designs incorporating nano- and micro-scale features can be used to tune the reaction kinetics of HER and OER processes.[24-25] For example, efficiency of OER in alkaline solutions can be impacted by electrochemically deposited Ni nano-structures [18, 22], incorporation of flower-like Ni particles[26], or Ni inverse opals.[23,27] Some of these electrode structures can improve the efficiency of OER through the use of randomly arranged structures created by direct electrodeposition, or the creation of structured surfaces using hydrogen bubbles of various diameters as negative templates.[18,22-25] A primary goal of our study is to prepare and evaluate Ni electrodes with well-defined, regularly spaced arrays of Ni micro-structures. We sought potential correlations between the morphology of these Ni electrodes and their OER efficiency in alkaline solutions.

In this study, we prepared Ni electrodes with regular arrays of cylindrical pillars or recessed features of an equivalent thickness, and evaluated their electrochemical performance in comparison to planar Ni electrodes. These arrays of micro-structured surfaces were defined by polymer templates patterned by photolithographic techniques, and the Ni structures were created by Ni electrodeposition through the polymer templates followed by selective removal of these templates. The physical dimensions and morphology of the structured Ni electrodes were characterized by scanning electron microscopy (SEM), and their wetting characteristics were determined by water contact angle (WCA) measurements. Electrochemical characterization of these electrodes included cyclic voltammetry (CV) for the determination of electrochemical surface area (A_{ecsa}), and OER performance as determined through linear sweep voltammetry (LSV), chronopotentiometry (CP), and chronoamperometry (CA) techniques.

2. Materials and Methods

2.1 Materials and Supplies

The KOH electrolyte used in this study was prepared from potassium hydroxide pellets (AR®, ACS grade) purchased from Avantor Performance Materials (PA, United States). A 6.35-mm diameter Ni 200 rod (99.6%) was purchased from Online Metals (www.onlinemetals.com) for making the Ni electrodes. The photolithography process used materials that included AZ® 1518 photoresist and MF-319 developer that were purchased from MicroChemicals GmbH (Germany); and chromium photomasks purchased from 4D LABS at Simon Fraser University (www.4dlabs.ca). Nickel electrodes used in this study were polished with materials purchased from Allied High Tech Products. The nickel Watts plating bath was purchased

from Transene Company (MA, United States). All electrochemical analytes were purged and a head space maintained with 99.998% purity N_2 (g) that was purchased from Praxair, Canada. All water used to prepare the necessary solutions and for rinsing of the electrodes was filtered with a Barnstead DIamond™ deionized water system with an output of 18 MΩ·cm.

2.2 Preparation of Structured Nickel Electrodes

The nickel rod was sectioned into smaller cylindrical sections, each with a length of 8 mm. The working ends of the Ni electrodes were polished to a mirror finish using a series of alumina polishing pastes with colloidal diameters of 5 μm, 0.3 μm, and 0.05 μm, respectively. The resulting polished Ni stubs were used as the substrates upon which all samples were prepared. The Ni electrodes containing regular arrays of pillared or recessed cylindrical structures were prepared by the following photolithography process: (1) spin cast AZ® 1518 photoresist (PR) onto the substrate at 4,000 rotations per minute (rpm); (2) place the desired Cr photomask onto the PR coated substrate and expose to UV light (365 nm; UVP® Blak-Ray B-100SP portable UV) for ~45 s; (3) develop the exposed PR by immersion in a solution of MF-319 developing solution for ~2 min, followed by rinsing with water; (4) assemble the Ni substrate with the patterned PR into a ChangeDisk (Pine Research Instrument, NC, United States) electrode holder; (5) immerse this assembly into the Ni plating bath and electrodeposit Ni onto the exposed regions of the Ni substrate at 5 mA/cm² for ~3 min; (6) inspect the deposited Ni substrate with a Zeiss Axio M1m optical microscope using a differential interference contrast filter to monitor the Ni deposition process and to initially assess the thickness of deposited Ni relative to that of the templates (step 5 was repeated if necessary); and (7) remove the PR with acetone to reveal the electrodeposited features. A schematic of the process to prepare structured Ni electrodes with regular arrays of cylindrical features is portrayed in Figure 1a.

2.3 Physical Characterization of Structured Nickel Electrodes

Scanning electron microscopy was used to inspect the morphology and dimensions of the electrodeposited Ni features. The SEM data were collected using an FEI Nova NanoSEM system operating at 10kV and using a secondary electron detector. Thickness of the electrodeposited Ni was verified by tilting each substrate by 55 degrees to inspect the side profile and heights of the cylindrical features. Water contact angles (WCAs) were obtained using a VCA Optima (AST Products, MA, United States) contact angle measurement instrument. The WCA of each electrode was measured 5 times by placing 1 μL water droplets at different locations on these electrodes. The WCA values were digitally determined using the AutoFAST imaging software.

2.4 Characterization of Composition of Structured Nickel Electrodes

X-ray photoelectron spectroscopy (XPS) was performed to verify the chemical composition of the Ni electrodes. These studies were conducted using a Kratos Analytical

Axis ULTRA DLD system with a monochromatic aluminum source (Al Kα of 1486.7 eV) operating at 150 W with a 90° take-off angle. Survey scans (0 to 1200 eV) were acquired using a pass energy of 160 eV, a dwell time of 100 ms, and 1 sweep. High resolution scans were obtained using a pass energy of 20 eV, a dwell time of 500 ms, and 15 sweeps. An area of 700 µm by 300 µm was analyzed in three separate regions of each sample to evaluate the uniformity of their surface composition. The XPS peak analysis and quantification of atomic composition, with appropriate relative sensitivity factors, was performed using Vision Processing software.
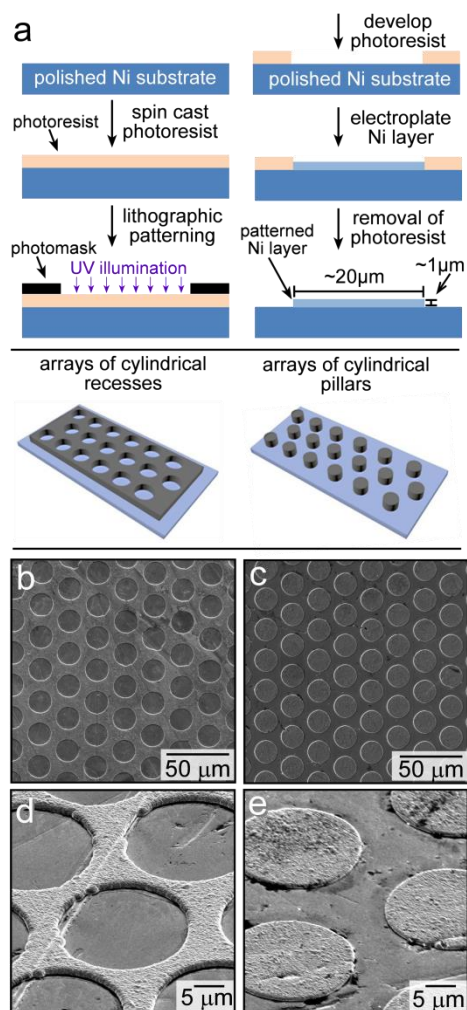

Figure 1. (a) A schematic depiction, drawn to proportion, of the photolithographic process used to prepare structured nickel electrodes. End of life scanning electron microscopy (SEM) images are included for (b) an array of recesses, each with a diameter (ø) of 20 µm, in a Ni film, and (c) an array of 20-µm ø Ni pillars. (d, e) Higher magnification SEM images were obtained at a tilt of 55 degrees (d, array of recesses; e, array of pillars).

2.5 Electrochemical Characterization of Structured Nickel Electrodes

A series of electrochemical experiments were performed to condition the electrodes for OER, to determine the A_{ecsa}

of the samples, and to determine the OER efficiency of the electrodes. These experiments were performed using a Bio-Logic Science Instruments SP-150 potentiostat in addition to an analytical rotating disk electrode (RDE) system (Modulated Speed Rotator, Pine Research Instrumentations, PA, United States). Electrochemical data was collected using EC-Lab data analysis software (V10.18). The prepared electrodes were incorporated as the working electrode into a typical three electrode set-up using a custom glass electrochemistry cell with a single junction, 10-mm diameter, Ag/AgCl reference electrode (Fisher Scientific™ accumet™ Single Junction Glass Body Ag/AgCl Reference Electrode), and a Ni (0.5-mm diameter; 99.994%; Alfa Aesar) wound wire counter electrode. All electrochemical experiments were performed in an 8 M KOH solution that was purged with N_2 (g) for at least 30 min prior to the commencement of the experiments. This concentration of KOH is in-alignment with concentrations commonly used for industrial alkaline electrolyzers and fuel regeneration systems associated with metal-air fuel cells.[15, 18-20] A positive N_2 atmosphere was maintained in the head space of the electrochemical cell throughout the experiments. Each Ni electrode surface was briefly rotated at 9,900 rpm and visually verified to be free of adsorbed surface bubbles. The CV measurements were performed at a scan rate of 100 mV/s, with a sweep range from –0.4 to 0.5 V, at an ambient temperature of 22.1°C ±0.2, and with a rotation speed of 800 rpm. The subsequent LSV experiments were performed with the same set-up, but at different rotation speeds and with potentials scanned from 0.3 to 0.7 V at a sweep rate of 5 mV/s. These parameters were chosen to assess the catalytic efficiency of OER for these electrodes in alkaline solutions. Further CP and CA experiments were performed by holding the working electrode at 100 mA/cm² or a 100 mV overpotential, respectively, for 10 min. Fourier transform analyses were performed using MATLAB (R2016a) to extract the frequencies of the current oscillations within the CA data.

3. Results and Discussion

3.1 Characterization of the Micro-structured Nickel Electrodes

Micro-structured Ni electrodes containing arrays of cylindrical features with a uniform diameter, spacing, and thickness were prepared for the evaluation of their OER performance. These regular arrays of cylindrical pillars or recesses, arranged in a hexagonal pattern, were prepared on the surfaces of polished Ni electrodes. These features are henceforth abbreviated as Ni recesses and Ni pillars. These cylindrical features had diameters of 20 µm and a minimum spacing of 7 µm between the features. The SEM analysis confirmed the regularity of these patterned arrays and also determined that the electrochemically deposited features had an average thickness of ~1 µm ±0.09 (Figures 1b-1e). Examples of the cross-sectional measurements obtained from a tilted view of the samples at high magnification analyses by SEM are presented in Figure S1. The uniform arrays of cylindrical features with regular spacing allow us to determine the theoretical increase in surface area (or theoretical surface roughness) of the electrodes. The Ni

pillars and Ni recesses were both prepared with consistent physical dimensions (i.e. the cylindrical features for each type of electrode had equivalent feature diameters, spacing, thickness, and percent surface area increase). The stringent control over electrode surface features enables us to observe bubble release dynamics that is affected solely by a single electrode surface parameter, where the only difference between the samples is the contrast in their surface features (i.e. pillars versus recesses). The lateral dimensions of the features were chosen due to its intermediate size to those reported in the literature. For example, porous Ni foams have been previously prepared by electrodepositing Ni through hydrogen gas bubble templates adsorbed onto the surfaces of an electrode.[23] These electrodes contained spherical pores with diameters from 650 nm to 100 μm, which exhibited an improved OER performance. In addition, the diameters of our cylindrical features is about one order of magnitude less than the estimated diameter of the oxygen bubbles at the point of detachment from planar electrode surfaces in alkaline analytes (i.e. 200 to 280 μm).[22] It was anticipated that larger surface features (in contrast to those <1 μm) may have more of an impact on bubble release dynamics and, therefore, the OER efficiencies of these electrodes might be improved. The low aspect ratios of the cylindrical features were chosen to minimize the surface roughness and potentially avoid trapping oxygen gas bubbles at the electrode surfaces.

The electrochemical active surface area (A_{ecsa}) was determined for each of our electrodes to assist in comparing the OER performance of each type of electrode. The A_{ecsa} of each sample was determined by integrating the area under the reduction peaks of the conditioned CV profiles. The total charge (area under the peak) was converted to A_{ecsa} using the assumption that the formation of one monolayer of α-Ni(OH)$_2$ has a surface charge of 514 μC /cm².[27-30] Due to the presence of both α-Ni(OH)$_2$ and β-Ni(OH)$_2$ on the conditioned Ni surfaces, the A_{ecsa} determined from the reduction peaks in the CV profiles might be underestimated.[30-31] Since the same method was used to determine A_{ecsa} for all the samples, the estimation of A_{ecsa} is self-consistent througout this study. Control samples were used to further assess changes in OER performance. A polished Ni electrode, as well as a planar Ni electrode coated with ~1 μm of electrodeposited Ni were used as standard samples. The SEM analysis of the electrodeposited Ni thin films indicated the presence of nanoscale roughness in contrast to the surface textures on the polished electrodes. Despite these differences in surface texture, these control samples had similar A_{ecsa} values (Table S1). These results suggest that differences in surface roughness observed in the SEM analysis only had a small impact (estimated to be ~7 %) on their electrochemical active surface areas. This similarity of the polished and electrodeposited planar Ni electrodes was further confirmed through LSV experiments, which will be discussed in further detail in the following section. The CV analysis suggested that the Ni pillars and Ni recesses exhibited an increase in A_{ecsa} of 55% and 34%, respectively. This variance in A_{ecsa} can be attributed to a combination of possible surface roughness differences, presence of adsorbed surface bubbles, and minor height differences between the electrodeposited pillar and recess features. The various forms of Ni exhibit different electrochemical stabilities and OER activities under alkaline conditions.[25,31-34] To minimize variability in the phases of Ni present at the surfaces of these electrodes, a minimum of 300 electrochemical cycles (cycled from −0.4 to 0.5 V versus Ag/AgCl) were applied to each electrode. This process transformed their surfaces to achieve a uniform Ni phase prior to assessing OER activities. Typical CV profiles obtained during the conditioning of an array of 20-μm diameter pillars are shown in Figure 2. This figure portrays a shift in position (from 0.25 to 0.28 V) of the Ni oxidation peak, which we hypothesize could be attributed to the following reasons: (1) It is possible that the initial cathodic peak (at 0.25 V versus Ag/AgCl) may be a partially oxidized form of α-Ni(OH)$_2$ under the highly alkaline conditions.[34] Due to the increased nanoscale roughness on the surfaces of the electrodeposited Ni and the cylindrical micro-structure features, the probable presence of trapped air bubbles, and the simultaneous generation of oxygen bubbles when scanning the potential, some of the α-Ni(OH)$_2$ may be difficult for the electrolyte to access. The relatively fast scan rate (100 mV/s) used in this study might also lead to insufficient mass transport of electrolyte into the microporous structure of the electrodes, which would hinder the complete oxidation of the electrode surfaces. Therefore, the oxidation of α-Ni(OH)$_2$ to β-Ni(OH)$_2$ might progress with subsequent scans of the potential, resulting in the observed shift in the cathodic peak. (2) It is possible that all of the α-Ni(OH)$_2$ was oxidized at much lower potentials (~-0.2 V versus Ag/AgCl) due to relatively high alkalinity of the analyte. A broad peak associated with this oxidation can be observed in the first profile in the CV analyses. This species is irreversibly oxidized and, therefore, absent in the profile of the second scan (Figures S2 and S3). The peak shift observed in Figure 2 could be due to the transformation of β-Ni(OH)$_2$ into β-Ni(OOH).[35-36] This growth of the oxide layer reaches an equilibrium state with progressive scans of the potential, which is indicated by obtaining consistent CV profiles after obtaining the 300th profile (Figure S3). The oxide layer could also become progressively more difficult to oxidize due to its increased thickness and formation of mesoporous structures within the oxide layer.[33] Therefore, the cathodic peak progressively shifts and then reaches a consistent position and intensity as observed with the increasing number of scans of the potential. Electrodes analyzed without going through the conditioning process exhibited a continuous increase in the measured OER overpotential during the CP experiments (Figure S4).
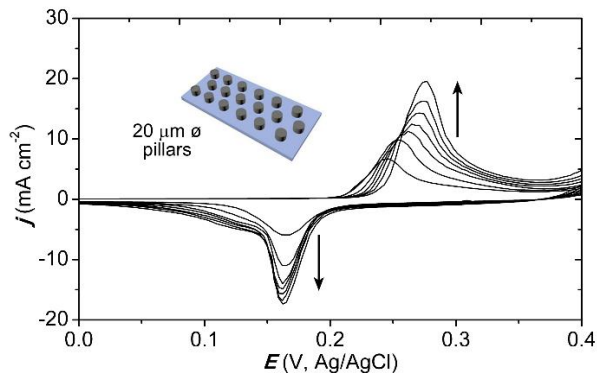
Figure 2. A series of overlaid cyclic voltammetry (CV) profiles obtained during oxidative conditioning of an array of 20-μm ø Ni pillars. Individual CV profiles are plotted at increments of ~40 cycles between the 1st and 300th profiles.

In addition to the phase of Ni present in the electrode surfaces, its elemental composition and purity can also influence the measured OER activity. For example, Ni-Fe can exhibit an increased OER activity in contrast to pure Ni.[37-41] Composition of our polished Ni electrodes and Ni electrodes with a thin film (~1 μm) of electrodeposited Ni (deposited from the commercial Watts bath) was confirmed through X-ray photoelectron spectroscopy (XPS) measurements (Figure S5). There was a trace presence of Fe in both types of Ni electrodes. The Ni electrode raw material (Ni 200) and the Watts Ni electrodeposition bath were specified to contain up to 1,200 and 6 ppm of Fe, respectively. The results from the LSV experiment described in the following section suggests that the potential difference in Fe content between the two types planar electrodes is not significant enough to result in substantial performance differences for OER throughout all rotational speeds (Figure 3a). It is possible that trace levels of Fe could also be present in the KOH electrolyte. The presence of any impurities in the electrolyte were consistent for all of the experiments. Previous studies suggest that the performance of Ni based electrodes for OER is similar at overpotentials of <250 mV despite significant differences in the Fe content of various samples (e.g., up to 50% Fe).[37] The following electrochemical analyses of the micro-structured Ni electrodes and planar control electrodes were performed at overpotentials of 100 mV to minimize any potential contributions from trace Fe when assessing their performance for OER.

3.2 Assessing the Oxygen Evolution Reaction for Micro-structured Nickel Electrodes

The OER activities of the micro-structured and planar Ni electrodes were determined through a series of RDE based LSV experiments. The electrodes were each rotated at a series of speeds from 500 to 8,900 rpm to determine their optimal rotation speed for mass transport. In between the LSV experiments at each rotational speed, bubbles adhered to the electrode surfaces were removed from the working electrode by briefly rotating the electrodes at 9,900 rpm.

This bubble removal process was directly followed by a series of five conditioning CV scans (as described in the Materials and Methods) to ensure electrochemical stability of the working electrodes, as well as to establish a consistent starting condition for each LSV experiment. The LSV experiments were performed in triplicate for each electrode and at each of the rotational speeds. Examples of Tafel plots derived for each of the electrodes at different rotational speeds are presented in Figure S6. For ease of comparing these results, the average current densities versus A_{ecsa} were obtained from the Tafel plots for each electrode at an overpotential of 100 mV (trends observed between each of the electrodes were consistent beyond this point) and plotted with respect to a series of rotational speeds (Figure 3). The electrodeposited Ni film exhibited a slight increase in the current density (<2 mA/cm²) when compared to the polished Ni electrode at rotational speeds from 500 to 1,300 rpm. The polished Ni electrode generally exhibited a larger relative increase in its current density when compared to the electrodeposited Ni film at rotational speeds from 2,100 to 8,900 rpm. The observed differences in performance of these planar electrodes were primarily attributed to the errors in the measured current densities as observed in the overlap of the calculated standard deviation from the mean values. The average 3-sigma standard deviation that accounts for 99.7% of the variation observed in the current density for the electrodeposited Ni film and the polished Ni throughout all of the rotational speeds (500 to 8,900 rpm) were 2.73 and 0.66 mA/cm², respectively. Despite the observed variation in current densities between the two electrodes, a significant increases (~4 times) in current density was observed for both electrodes at higher rotational speeds (>3,000 rpm) when compared to values obtained at lower rotational speeds (<1,300 rpm). This phenomenon could indicate that there is a mass transport limitation at lower rotational speeds for these electrodes (Figure 3a). The two planar electrodes exhibited a significant difference in their current density at a rotational speed of 3,400 rpm. According to the trend observed for an increasing current density with rotational speed, this rotational speed appears to be at the threshold of the observed mass transport limitations. It is possible that the electrodeposited Ni has a transition at slightly lower rotational speeds (e.g., at 3,000 rpm) than the polished Ni due to the slight difference in their surface roughness. This variation may result in the significant difference in current densities observed at the rotational speed of 3,400 rpm.

A similar trend of increasing current density at higher rotational speeds was also observed in the LSV experiments for the arrays of Ni pillars (Figure 3b). The increase in OER current density as a function of increasing rotational speeds was more gradual for the arrays of Ni pillars than that observed for the planar Ni electrodes.
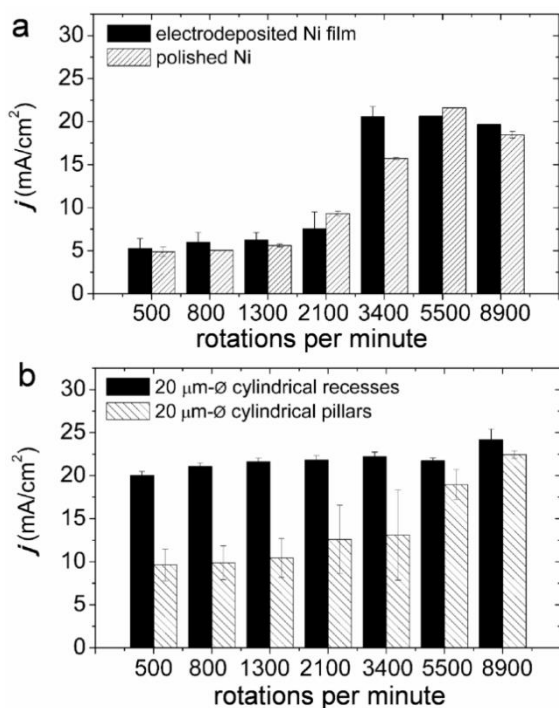
Figure 3. Specific current densities measured at an overpotential of 100 mV as a function of rotational speed for (a) planar Ni films obtained by either electrodeposition or mechanical polishing, and (b) structured Ni electrodes containing an array of either 20-μm diameter cylindrical recesses or cylindrical pillars. The error bars represent a 1σ variation in the measured current.

The OER current density for the Ni pillars was, however, nearly twice the values of the planar electrodes at rotational speeds from 500 to 1,300 rpm. The current density differences among these electrodes gradually diminished and reached similar maximum values as the rotational speed was increased from 2,100 to 8,900 rpm. This increase in OER current density for the Ni pillars at the lower rotational speeds when compared to the planar electrodes may be the result of a combination of effects. The Ni pillars could exhibit an increase in the lateral shear flow in between the surface micro-structures, resulting in an improved reagent flux, increased removal of the dissolved oxygen by-product, and reduced bubble adhesion at the electrode surfaces.[42]

The Ni pillar and Ni planar electrodes both exhibited an enhanced current density for OER at an overpotential of 100 mV as a function of rotational speed in comparison to the planar electrodes. A different phenomenon was, however, observed for the arrays of micro-structured recesses in comparison to the other types of Ni electrodes. The Ni recesses exhibited excellent OER activity at rotation speeds as low as 500 rpm. These results indicated that the Ni recesses had better mass transport (i.e., bubble release) properties in comparison to the other Ni electrodes. The fluid dynamic stability of gas bubbles in a liquid medium can be estimated by Weber number calculations. This model has been shown to successfully describe critical bubble dimensions leading to either a disintegration in size or bubble coalescence.[41,43-44] A Weber number was calculated for the Ni recesses and Ni pillars (Figure S7) to demonstrate the theoretical stabilities of O_2 bubbles formed on each of the electrodes. The characteristic length used in these calculations was assessed as the separations between the recessed features observed in a cross-sectional profile of each electrode (i.e. 20 μm for the Ni recesses, and 7 μm for the Ni pillars). The trend in the Weber number agreed with the observed OER activity of these electrodes. The O_2 bubbles formed in the Ni recesses were predicted to be less stable than the bubbles that were formed in between the Ni pillars. The predicted destabilization of O_2 bubbles for the arrays of Ni recesses agrees with the observed higher OER current density for these surfaces at reduced electrode rotational speeds, where the arrays of Ni recesses were 2 times more active than the arrays of Ni pillars. The WCA measurements that assessed the wetting properties of these electrode surfaces also indicated that the Ni pillars were more hydrophobic (WCA= 88°) than the Ni recesses (WCA= 83°) (Figure S8). These additional results suggested that the Ni pillars may have a higher tendency than the recesses to trap oxygen bubbles at the interface between the electrode and the electrolyte.

To further assess the electrochemical characteristics of the micro-structured Ni electrodes, constant potential CA experiments were performed at the same rotational speeds as the LSV experiments. The outcome of the LSV experiments only provides a "snapshot" of the efficiency of each electrode at a given potential and at a particular instance in time. Although this method serves as a quick technique for characterizing each of the electrode's performance towards OER as a function of rotational speed, the complete dynamics of bubble release might not be fully understood from these experiments. Constant potential CA experiments were, therefore, performed over longer durations for both the cylindrical pillars and recesses to assess their steady state OER performance. Data was collected over a duration of 10 min for each rotational speed. A Levich plot was constructed from experimental data using the current averaged from each CA profile between 560 and 600 s. This resulting plot allows a visual identification of the different mass transport characteristics of the electrodes containing Ni pillars and Ni recesses (Figure 4a). The Levich relationship for these two samples clearly indicates an improvement in mass transport for the Ni pillars at higher rotational speeds. The Ni recesses demonstrated a relatively linear relationship across the range of rotational speeds. At higher rotational speeds, the Ni pillars exhibited higher activities than the Ni recesses. In contrast, the LSV experiments presented in Figure 3b demonstrate that the Ni recesses exhibited higher current densities at all the rotational speeds than the Ni pillars. These conflicting results suggests that these electrodes require an equilibration period to stabilize the OER current density. In addition, the higher OER performance of the arrays of Ni pillars at higher rotational speeds may be due, in part, to the fact that at higher rotational speeds the bubbles near the electrodes may act as reservoirs for the uptake of dissolved oxygen gas and smaller bubbles. A small amount of oxygen

bubbles that remain adhered to the Ni surfaces may be beneficial for enhancing OER activity at the higher mass transport regime.[45-47]
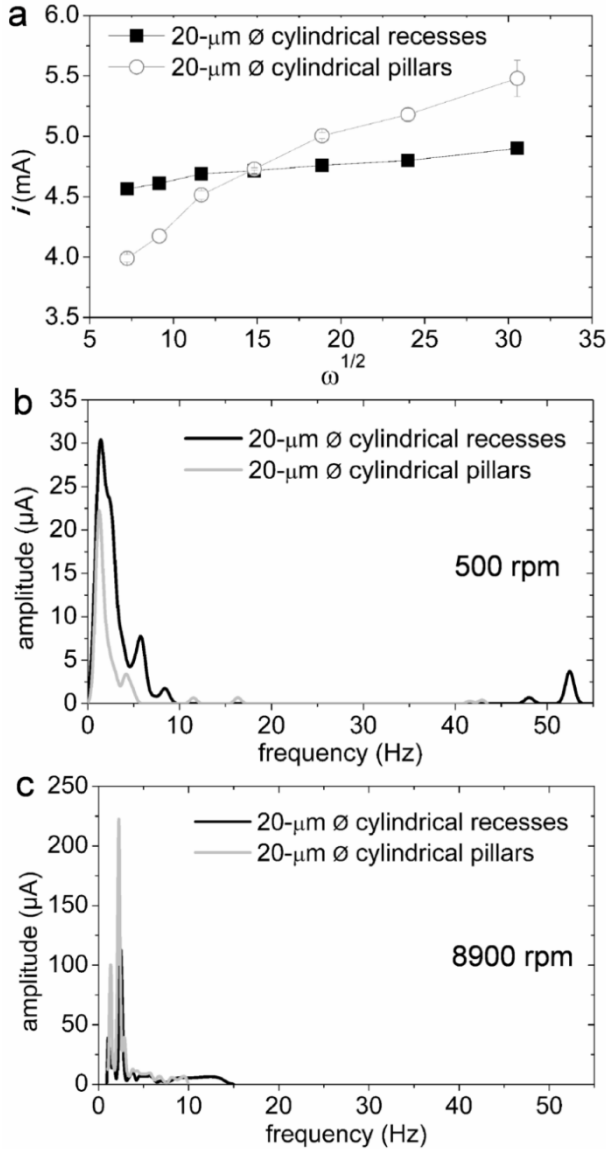

Figure 4. (a) Levich plots for the structured Ni electrodes at an overpotential of 100 mV. The error bars represent a 1σ variation in the measured current at steady state. (b, c) Fourier transforms of the chronoamperometric profiles for arrays of 20-μm ø cylindrical pillars and cylindrical recesses measured at an overpotential of 100 mV and at either a (b) low or (c) high rotation speed as indicated in each plot.

The bubble release characteristics of micro-structured electrodes were further determined by analyzing the oscillations in the measured currents during the CA experiments. Previous literature suggests that these oscillations correlate with bubble release events from the electrode surfaces.[37,48] The gradual accumulation of bubbles on the electrodes can impede reactants from reaching the electrode surfaces, which leads to a gradual decrease in current. An increase in bubble size destabilizes a bubble, which can lead to release of the bubble from the electrode surfaces. This release restores the A_{ecsa} that was blocked by

the bubble with a corresponding increase in the measured current. The dynamics of bubble release were further analyzed by extracting the frequencies and their corresponding magnitudes from the observed oscillations in current through a process of fitting the CA profiles followed by Fourier transformation of these waveforms (Figures 4b-c). This analysis depicted significant differences in the frequencies of oscillation in the current when comparing the Ni recesses to Ni pillars. The larger oscillations in current amplitude could correspond to the formation and release of larger bubbles at the surfaces, and the frequency of the oscillations could correlate to the rate of bubble release from the surfaces. Each type of electrode that exhibited larger oscillations in its current amplitudes corresponded to better OER activity according to the Levich plot (i.e. at lower rotational speeds for the Ni recesses and higher rotational speeds for the Ni pillars). A higher frequency of oscillations in current corresponded to improved OER performance at low rotational speeds, where adhered bubbles are not readily removed by the relatively low shear flows of analyte. The electrodes with lower frequencies in their observed oscillations in current only exhibited a higher OER activity at higher rotational speeds, where persistent bubbles attached to the surfaces could serve as favorable oxygen reservoirs. These findings along with the aforementioned results of the LSV, Levich, and Weber analyses, indicate that the Ni recesses exhibit a lower adhesion to the oxygen bubbles that resulted in a more frequent release of bubbles from their surfaces. At lower rotational speeds, this destabilization of the adhered bubbles promotes the simultaneous release of multiple bubbles or the release of larger bubbles from the surfaces. On the other hand, bubbles formed on the arrays of pillars, with their reduced critical dimension of separation between their features (i.e. 7 μm separation of the pillars), were not as readily removed at lower rotational speeds. However, at higher rotational speeds, where most bubbles adhered to the electrodes are destabilized, the increased bubble adhesion and the subsequent release of potentially larger bubbles was demonstrated to be beneficial to electrode performance for OER.

The results from this study suggest that an electrode with a lower adhesion to bubbles is optimal for gas generation at low analyte perturbation. Electrodes with a higher adhesion to bubbles is optimal for systems with a higher shear flows across the electrode surfaces. The electrode wettability and surface morphology should be tailored to their intended applications, such as OER for ZAFC regeneration and water electrolysis. It has been previously demonstrated that surfaces with hierarchically arranged nano- and micro-structures can possess variable wetting properties.[49-51] Surfaces with a balance of adhesion to both oxygen bubbles and electrolyte may futher improve electrode performance for OER. Future studies will utilize hierarchical structures to seek an optimal electrode surface morphology for OER.

4. Conclusion

It was demonstrated in this study that Ni micro-structured electrodes can have a positive impact on OER performance in contrast to planar Ni electrodes. The morphology

of the Ni electrodes can enhance the mass transfer and activities of OER. For example, uniform arrays of micro-scale Ni recesses and Ni pillars had excellent OER mass transport at low and high analyte perturbations, respectively. These micro-structured Ni electrodes could be utilized in water electrolysis systems (e.g., for generating fuel for PEMFCs), as well as fuel regeneration for ZAFCs. These structured electrodes could enhance bubble release, reducing the reaction overpotential for an overall more efficient generation of the requisite fuels. The improvement of OER activities with the inclusion of patterned, uniform arrays of micro-structures on Ni electrodes warrants a more detailed investigation by the field into the influences of micro-scale features on mass transport, bubble release and other aspect of electrochemical gas evolution reactions. Further improvements in the efficiency of these processes may result from additional studies into structure property correlations.

ASSOCIATED CONTENT

Additional details on the SEM tilted cross-sectional measurements, additional CV profiles, electrochemical surface areas, CA profiles, XPS data, Weber number analysis, and WCA results are presented in a Supporting Information document that is available free of charge via the Internet at http://pubs.acs.org.

AUTHOR INFORMATION

Corresponding Author

* To whom correspondence should be addressed. Email: bgates@sfu.ca Tel. (+1) 778-782-8066. Fax. (+1) 778-782-3765.

Author Contributions

The manuscript was written through contributions of all authors. All authors have given approval to the final version of the manuscript.

ACKNOWLEDGMENT

ABBREVIATIONS

A_{ecsa}, electrochemical surface area
CA, chronoamperometry
Cr, chromium
CP, chronopotentiometry
CV, cyclic voltammetry
LSV, linear sweep voltammetry
Ni, nickel
OER, oxygen evolution reaction
PEMFC, proton exchange membrane fuel cell
PR, photoresist
SEM, scanning electron microscopy
UV, ultraviolet
WCA, water contact angle
XPS, X-ray photoelectron spectroscopy

REFERENCES

(1) Linic, S.; Christopher, P.; Ingram, D. B., Plasmonic-Metal Nanostructures for Efficient Conversion of Solar to Chemical Energy. *Nat. Mater.* **2011,** *10* (12), 911-921.

(2) Kamat, P. V., Meeting the Clean Energy Demand: Nanostructure Architectures for Solar Energy Conversion. *J. Phys. Chem. C* **2007,** *111* (7), 2834-2860.

(3) Marvel, K.; Kravitz, B.; Caldeira, K., Geophysical Limits to Global Wind Power. *Nat. Clim. Change* **2013,** *3* (2), 118-121.

(4) Carrasco, J. M.; Franquelo, L. G.; Bialasiewicz, J. T.; Galvan, E.; Guisado, R. C. P.; Prats, A. M.; Leon, J. I.; Moreno-Alfonso, N., Power-Electronic Systems for the Grid Integration of Renewable Energy Sources: a Survey. *IEEE Trans. Ind. Electron.* **2006,** *53* (4), 1002-1016.

(5) Share, K.; Westover, A.; Li, M. Y.; Pint, C. L., Surface Engineering of Nanomaterials for Improved Energy Storage - A Review. *Chem. Eng. Sci.* **2016,** 154, 3-19.

(6) Kudo, A.; Miseki, Y., Heterogeneous Photocatalyst Materials for Water Splitting. *Chem. Soc. Rev.* **2009,** *38* (1), 253-278.

(7) Swisher, R.; De Azua, C. R.; Clendenin, J., Strong Winds on the Horizon: Wind Power Comes of Age. *Proc. IEEE* **2001,** *89* (12), 1757-1764.

(8) Zahedi, A.; Inst. Elect Engineers, H. K., *Combination of Renewable Sources of Energy And Energy Storage Units for Providing a Reliable Power Supply for Remote and Isolated Areas.* Inst. Electrical Engineers Inspec. Inc.: Edison, **1997**; p 559-562.

(9) Schlapbach, L.; Zuttel, A., Hydrogen-Storage Materials for Mobile Applications. *Nature* **2001,** *414* (6861), 353-358.

(10) Arico, A. S.; Bruce, P.; Scrosati, B.; Tarascon, J. M.; Van Schalkwijk, W., Nanostructured Materials for Advanced Energy Conversion and Storage Devices. *Nat. Mater.* **2005,** *4* (5), 366-377.

(11) Diat, O.; Gebel, G., Fuel Cells: Proton Channels. *Nat. Mater.* **2008,** *7* (1), 13-14.

(12) Koczara, W.; Chlodnicki, Z.; Al-Khayat, N.; Brown, N. L., *Energy Management and Power Flow of Decoupled Generation System for Power Conditioning of Renewable Energy Sources.* IEEE: New York, **2008**; p 2150-2155.

(13) Soberanis, M. A. E.; Fernandez, A. M., A Review on the Technical Adaptations for Internal Combustion Engines to Operate with Gas/Hydrogen Mixtures. *Int. J. Hydrogen Energy* **2010,** *35* (21), 12134-12140.

(14) Taylor, E. J.; Anderson, E. B.; Vilambi, N. R. K., Preparation of High-Platinum-Utilization Gas-Diffusion Electrodes for Proton-Exchange-Membrane Fuel-Cells. *J. Electrochem. Soc.* **1992,** *139* (5), 45-46.

(15) Neburchilov, V.; Wang, H. J.; Martin, J. J.; Qu, W., A Review on Air Cathodes for Zinc-Air Fuel Cells. *J. Power Sources* **2010,** *195* (5), 1271-1291.

(16) Sapkota, P.; Kim, H., Zinc-Air Fuel Cell, a Potential Candidate for Alternative Energy. *J. Ind. Eng. Chem.* **2009,** *15* (4), 445-450.

(17) Smedley, S. I.; Zhang, X. G., A Regenerative Zinc-Air Fuel Cell. *J. Power Sources* **2007,** *165* (2), 897-904.

(18) Ahn, S. H.; Choi, I.; Park, H. Y.; Hwang, S. J.; Yoo, S. J.; Cho, E.; Kim, H. J.; Henkensmeier, D.; Nam, S. W.; Kim, S. K.; Jang, J. H., Effect of Morphology of Electrodeposited Ni Catalysts on the Behavior of Bubbles Generated During the Oxygen Evolution Reaction in Alkaline Water Electrolysis. *Chem. Commun.* **2013**, *49* (81), 9323-9325.

(19) Matsushima, H.; Nishida, T.; Konishi, Y.; Fukunaka, Y.; Ito, Y.; Kuribayashi, K., Water Electrolysis under Microgravity - Part 1. Experimental Technique. *Electrochim. Acta* **2003**, *48* (28), 4119-4125.

(20) Zeng, K.; Zhang, D. K., Recent Progress in Alkaline Water Electrolysis for Hydrogen Production and Applications. *Prog. Energy Combust. Sci.* **2010**, *36* (3), 307-326.

(21) Lu, X. Y.; Zhao, C. A., Electrodeposition of Hierarchically Structured Three-Dimensional Nickel-Iron Electrodes for Efficient Oxygen Evolution at High Current Densities. *Nat. Commun.* **2015**, *6*, 7.

(22) Huet, F.; Musiani, M.; Nogueira, R. P., Oxygen Evolution on Electrodes of Different Roughness: an Electrochemical Noise Study. *J. Solid State Electrochem.* **2004**, *8* (10), 786-793.

(23) Huang, Y. J.; Lai, C. H.; Wu, P. W.; Chen, L. Y., Ni Inverse Opals for Water Electrolysis in an Alkaline Electrolyte. *J. Electrochem. Soc.* **2010**, *157* (3), 18-22.

(24) Ahn, S. H.; Hwang, S. J.; Yoo, S. J.; Choi, I.; Kim, H. J.; Jang, J. H.; Nam, S. W.; Lim, T. H.; Lim, T.; Kim, S. K.; Kim, J. J., Electrodeposited Ni Dendrites with High Activity and Durability for Hydrogen Evolution Reaction in Alkaline Water Electrolysis. *J. Mater. Chem.* **2012**, *22* (30), 15153-15159.

(25) Gao, M. R.; Sheng, W. C.; Zhuang, Z. B.; Fang, Q. R.; Gu, S.; Jiang, J.; Yan, Y. S., Efficient Water Oxidation Using Nanostructured Alpha-Nickel-Hydroxide as an Electrocatalyst. *J. Am. Chem. Soc.* **2014**, *136* (19), 7077-7084.

(26) Xu, L. P.; Ding, Y. S.; Chen, C. H.; Zhao, L. L.; Rimkus, C.; Joesten, R.; Suib, S. L., 3D Flowerlike Alpha-Nickel Hydroxide with Enhanced Electrochemical Activity Synthesized by Microwave-Assisted Hydrothermal Method. *Chem. Mater.* **2008**, *20* (1), 308-316.

(27) Williams, V. O.; DeMarco, E. J.; Katz, M. J.; Libera, J. A.; Riha, S. C.; Kim, D. W.; Avila, J. R.; Martinson, A. B. F.; Elam, J. W.; Pellin, M. J.; Farha, O. K.; Hupp, J. T., Fabrication of Transparent-Conducting-Oxide-Coated Inverse Opals as Mesostructured Architectures for Electrocatalysis Applications: a Case Study with NiO. *ACS Appl. Mater. Interfaces* **2014**, *6* (15), 12290-12294.

(28) Grdeń, M.; Alsabet, M.; Jerkiewicz, G., Surface Science and Electrochemical Analysis of Nickel Foams. *ACS Appl. Mater. Interfaces* **2012**, *4* (6), 3012-3021.

(29) van Drunen, J.; Kinkead, B.; Wang, M. C. P.; Sourty, E.; Gates, B. D.; Jerkiewicz, G., Comprehensive Structural, Surface-Chemical and Electrochemical Characterization of Nickel-Based Metallic Foams. *ACS Appl. Mater. Interfaces* **2013**, *5* (14), 6712-6722.

(30) van Drunen, J.; Barbosa, A. F. B.; Tremiliosi, G., The Formation of Surface Oxides on Nickel in Oxalate-Containing Alkaline Media. *Electrocatalysis* **2015**, *6* (5), 481-491.

(31) Hall, D. S.; Bock, C.; MacDougall, B. R., An Oxalate Method for Measuring the Surface Area of Nickel Electrodes. *J. Electrochem. Soc.* **2014**, *161* (12), 787-795.

(32) Oliva, P.; Leonardi, J.; Laurent, J. F.; Delmas, C.; Braconnier, J. J.; Figlarz, M.; Fievet, F.; Deguibert, A., Review of the Structure and the Electrochemistry of Nickel Hydroxides and Oxy-Hydroxides. *J. Power Sources* **1982**, *8* (2-3), 229-255.

(33) Medway, S. L.; Lucas, C. A.; Kowal, A.; Nichols, R. J.; Johnson, D., In Situ Studies of the Oxidation of Nickel Electrodes in Alkaline Solution. *J. Electroanal. Chem.* **2006**, *587* (1), 172-181.

(34) Godwin, I. J.; Lyons, M. E. G., Enhanced Oxygen Evolution at Hydrous Nickel Oxide Electrodes via Electrochemical Ageing in Alkaline Solution. *Electrochem. Commun.* **2013**, *32*, 39-42.

(35) Alsabet, M.; Grden, M.; Jerkiewicz, G., Electrochemical Growth of Surface Oxides on Nickel. Part 2: Formation of B-$Ni(OH)_2$ and NiO in Relation to the Polarization Potential, Polarization Time, and Temperature. *Electrocatalysis* **2014**, *5* (2), 136-147.

(36) Kibria, M. F.; Mridha, M. S., Electrochemical Studies of the Nickel Electrode for the Oxygen Evolution Reaction. *Int. J. Hydrogen Energy* **1996**, *21* (3), 179-182.

(37) Corrigan, D. A., The Catalysis of the Oxygen Evolution Reaction by Iron Impurities in Thin-Film Nickel-Oxide Electrodes. *J. Electrochem. Soc.* **1987**, *134* (2), 377-384.

(38) Michael, J. D.; Demeter, E. L.; Illes, S. M.; Fan, Q. Q.; Boes, J. R.; Kitchin, J. R., Alkaline Electrolyte and Fe Impurity Effects on the Performance and Active-Phase Structure of NiOOH Thin Films for OER Catalysis Applications. *J. Phys. Chem. C* **2015**, *119* (21), 11475-11481.

(39) Trotochaud, L.; Young, S. L.; Ranney, J. K.; Boettcher, S. W., Nickel-Iron Oxyhydroxide Oxygen-Evolution Electrocatalysts: The Role of Intentional and Incidental Iron Incorporation. *J. Am. Chem. Soc.* **2014**, *136* (18), 6744-6753.

(40) Enman, L. J.; Burke, M. S.; Batchellor, A. S.; Boettcher, S. W., Effects of Intentionally Incorporated Metal Cations on the Oxygen Evolution Electrocatalytic Activity of Nickel (Oxy)hydroxide in Alkaline Media. *ACS Catal.* **2016**, *6* (4), 2416-2423.

(41) Martinez-Bazan, C; Montanes, J.L; Lasheras, J.C., On the Breakup of an Air Bubble Injected Into a Fully Developed Turbulent Flow. Part 1. Breakup Frequency. *J. Fluid Mech.* **1999**, *401*, 157-182.

(42) Kadyk, T.; Bruce D.; Eikerling, M., How to Enhance Gas Removal from Porous Electrodes? *Sci. Reports* **2016**, 6, 38780

(43) Kushch, V.I.; Sangani, A.S.; Spelt, P.D.M.; Koch, D.L., Finite-Weber-Number Motion of Bubbles Through a Nearly Inviscid Liquid. *J. Fluid Mech.* **2002**, *460*, 241-280.

(44) Qian, D.; McLaughlin, J.B., Simulation of Bubble Breakup Dynamics in Homogeneous Turbulence. *Chem. Eng. Commun.* **2006**, *193*, 1038-1063.

(45) Eigeldinger, J.; Vogt, H., The Bubble Coverage of Gas-Evolving Electrodes in a Flowing Electrolyte. *Electrochim. Acta* **2000**, *45* (27), 4449-4456.

(46) Vogt, H.; Balzer, R. J., The Bubble Coverage of Gas-Evolving Electrodes in Stagnant Electrolytes. *Electrochim. Acta* **2005**, *50* (10), 2073-2079.

(47) Balzer, R. J.; Vogt, H., Effect of Electrolyte Flow on the Bubble Coverage of Vertical Gas-Evolving Electrodes. *J. Electrochem. Soc.* **2003**, *150* (1), 11-16.

(48) Li, F. B.; Lubetkin, S. D.; Roberts, D. J.; Hillman, A. R., Electrogravimetric and Chronoamperometric Monitoring of Individual Events of Growth and Detachment of Electrolytic Chlorine Gas-Bubbles. *J. Chem. Soc., Chem. Commun.* **1994**, (2), 159-160.

(49) Bormashenko, E.; Starov, V., Impact of Surface Forces on Wetting of Hierarchical Surfaces and Contact Angle Hysteresis. *Colloid Polym. Sci.* **2013**, *291* (2), 343-346.

(50) Kavousanakis, M. E.; Chamakos, N. T.; Papathanasiou, A. G., Connection of Intrinsic Wettability and Surface Topography with the Apparent Wetting Behavior and Adhesion Properties. *J. Phys. Chem. C* **2015**, *119* (27), 15056-15066.

(51) Paul, M. T. Y.; Gates, B. D., Hierarchical Surface Coatings of Polystyrene Nanofibers and Silica Microparticles with Rose Petal Wetting Properties. *Colloids Surf., A* **2016**, *498*, 42-49.

Table of contents image

arrays of cylindrical recesses

arrays of cylindrical pillars

50 μm

50 μm

- ■ 20-μm Ø cylindrical recesses
- ○ 20-μm Ø cylindrical pillars

i (mA)

$\omega^{1/2}$